Pergamon

Int. J. Heat Mass Transfer. Vol. 40, No. 2, pp. 247–267, 1997

0017 9310/97 $15.00 + 0.00

PII: S0017-9310(96)00119-6

Mapping of impact and heat transfer regimes of water drops impinging on a polished surface

JOHN D. BERNARDIN, CLINTON J. STEBBINS and ISSAM MUDAWAR†

Boiling and Two-Phase Flow Laboratory, School of Mechanical Engineering, Purdue University, West Lafayette, IN 47907, U.S.A.

(*Received* 11 *September* 1995 *and in final form* 27 *March* 1996)

Abstract—Still and high-speed photographic techniques were used to record the impact behavior of water droplets on a hot aluminum surface. Drop velocity and surface temperature were two important parameters governing both the impact behavior and ensuing heat transfer. Droplet Weber numbers of 20, 60 and 220 identified three major classes of impact behavior, while surface temperatures ranging from 280 to 100°C were used to define heat transfer regimes corresponding to film boiling, transition boiling, nucleate boiling, and film evaporation. Temperatures corresponding to the critical heat flux and the Leidenfrost point showed little sensitivity to both droplet velocity and impact frequency. The photographic results and heat transfer measurements were used to construct droplet impact regime maps which identify the various boiling regimes for each of the three Weber numbers. These maps serve as a new useful foundation for understanding droplet impact behavior as well as future analytical or numerical modeling of droplet and spray heat transfer. Copyright © 1996 Elsevier Science Ltd.

1. INTRODUCTION

Intense cooling is widely used in two main types of applications, those demanding rapid cooling from high temperatures, such as quenching of aluminum and steel, and those requiring steady removal of concentrated heat loads, such as the cooling of lasers and electronic devices. Recent advances in these applications are demanding both enhanced heat removal rates and better surface temperature control. While flow boiling techniques such as jet impingement have shown promising results in dissipating high heat fluxes, they produce very uneven cooling because of the large spatial variations in heat flux between the impingement zone and surrounding surface. Not only does spray boiling greatly increase spatial cooling uniformity relative to jet impingement, but it also offers the benefits of adaptability to different cooling situations as well as savings in flow rate requirements.

These attributes have made spray cooling the method of choice in many heat treating operations, especially those involving aluminum alloys. During solution heat treating, metallic alloy parts are first preheated to a temperature slightly below the melting point in order to dissolve the alloy solutes into the primary metal matrix (aluminum). The part is then rapidly quenched in order to freeze the solid microstructure attained during the preheating process. Finally, the part is reheated to some intermediate temperature to allow the hardening solutes to coalesce into sites which are finely and uniformly dispersed within the grains of the primary metal. These finely dispersed solutes act as dislocation barriers, resisting deformations resulting from externally applied forces and resulting in a material with high strength and hardness.

Slow (poor) quenching can have disastrous consequences in heat treating, as it may allow massive precipitation of the solutes along grain boundaries instead of fine dispersion within the grains themselves. The result is a material with very poor strength and hardness. Therefore, the implementation of spray cooling in any heat treating operation demands a systematic methodology for predicting both the temporal and spatial variations of heat flux across the spray impact area.

Boiling curve vs cooling curve

To understand how variations of the cooling heat flux influence metallurgical microstructure and resulting material properties, consider first the simple reference case of a small (isothermal) mass being quenched from a high initial temperature in a stagnant bath of liquid. As the liquid comes into contact with the hot surface, the heat transfer rate is governed by fluid and solid thermal properties as well as surface roughness and temperature. The surface temperature is generally noted as the single most important parameter in quenching and is used to define the four distinct heat transfer regimes of the boiling curve as shown in Fig. 1a: (1) film boiling, (2) transition boiling, (3) nucleate boiling, and (4) single-phase liquid cooling. Interestingly, as will be illustrated later, the general shape of the boiling curve for a spray is very similar to that for a stagnant bath.

While the boiling curve has found wide use in most

† Author to whom correspondence should be addressed.

NOMENCLATURE

a, b	empirical constants
c_p	specific heat
d_o	droplet diameter just prior to impact
k	thermal conductivity
R	film radius
Re	droplet Reynolds number $(\rho_f u_o d_o/\mu_f)$
R_{max}	maximum film radius
r_o	droplet radius just prior to impact
T	temperature
t	time from onset of impact
t_{max}	time from onset of impact to instant of maximum film spread
t^+	normalized time parameter (d_o/u_o)
u_o	droplet velocity just prior to impact
We	droplet Weber number $(\rho_f u_o^2 d_o/\sigma)$.

Greek symbols

ΔT_{sat}	excess liquid saturation temperature $(T_s - T_{sat})$
μ	viscosity
ρ	density
σ	surface tension
τ_c	contact period from onset of impact to onset of rebound
τ_i	period from onset of impact to boiling incipience
ϕ_c^*	nondimensional height of drop/film.

Subscripts

CHF	critical heat flux
f	liquid
MIN	minimum heat flux (Leidenfrost condition for droplets)
o	initial
s	solid surface.

boiling studies, the temperature–time or cooling curve shown in Fig. 1b is more frequently used in quenching studies. The curve displays the cooling history for the surface and exhibits the four heat transfer regimes identified on the boiling curve. The patterns of liquid–surface contact and ensuing heat transfer are characteristically different in each of the four regimes. Cooling commences at a relatively slow rate in the film boiling regime, where the liquid is separated from the surface by a continuous vapor blanket. Liquid–solid contact, both partial in the transition boiling regime and more abundant in the nucleate boiling regime, greatly accelerates the cooling process in the respective regimes. Cooling finally subsides in the single-phase liquid cooling regime as bubble activity completely ceases.

As will be illustrated later, the cooling curve for a spray-quenched surface is similar in shape to that for bath quenching despite drastic differences in the liquid–solid contact pattern between the two cases. As in bath quenching, spray quenching commences with a relatively slow rate of cooling, apparently due to a very rapid development of a thin vapor layer which cushions the spray droplets from the surface upon impact. The film boiling regime persists from elevated surface temperatures down to a lower limit commonly referred to as the minimum heat flux or Leidenfrost point (LFP). Below this temperature limit exists the transition boiling regime, in which the droplets begin to effectively wet the surface resulting in higher heat transfer rates and a faster decrease in the surface temperature. As the surface temperature decreases in the transition boiling regime from the LFP, the heat transfer rate increases as more efficient surface wetting and boiling occur. At the lower temperature boundary of the transition boiling regime, the critical heat flux (CHF), virtually the entire surface becomes available for wetting by liquid and heat transfer rate reaches a maximum. This maximum heat flux point corresponds to the inflection point or the steepest portion of the cooling curve. In the nucleate boiling regime below the CHF temperature, heat transfer rate decreases with decreasing surface temperature as bubble formation becomes less abundant. The lower boundary of the nucleate boiling regime is determined by the minimum surface superheat required to sustain vapor bubble nucleation and growth within the impinging droplets. Below this limit exists the film evaporation regime which replaces the single-phase liquid cooling regime associated with bath quenching. In this regime, heat from the surface is conducted through the liquid film and dissipated by evaporation at the liquid–gas interface. This regime, which is characterized by long evaporation times, can exist even several degrees above the liquid saturation temperature, depending on the surface roughness and liquid properties.

The aforementioned detrimental precipitation of solutes along grain boundaries which results from poor quenching in heat treating operations is primarily the result of the poor heat transfer rate associated with film boiling, as virtually all of this precipitation occurs at high temperatures corresponding to the film boiling regime [1, 2]. Two methods of precluding such massive precipitation are to increase the cooling rate associated with the film boiling regime or to attain the Leidenfrost condition at relatively high temperatures, in order to take advantage of the faster cooling rate possible in the transition boiling regime.

Despite similarities in the shapes of the boiling curve

and cooling curve for spray quenching compared to those for bath quenching, there exist many fundamental differences. The spray liquid comes into contact with the solid surface in the form of discrete droplets which can be statistically characterized with respect to diameter and velocity. The rate of droplet arrival per unit area is governed by an important spray parameter called volumetric flux (volume flow rate of spray liquid per unit area per unit time). While significant work has been performed in the past to correlate data for single droplet impact or for sprays, to the authors' knowledge, no-one has successfully bridged the gap between the two extremes in pursuit of a closure model for spray cooling. In the next section, literature concerning droplet heat transfer will be reviewed and the fundamental questions pertaining to this type of closure modeling identified as a basis for the present work.

Droplet impact literature

Most of the research performed in the area of spray heat transfer has been empirical in nature. While the results from such studies may be beneficial for specific applications, they are generally lacking in general applicability. This review begins with a discussion of the important issues involved with the fluid and heat transfer characteristics of both sessile (stationary) and impinging droplets.

Sessile droplet behavior has been investigated extensively by several researchers. Analytical

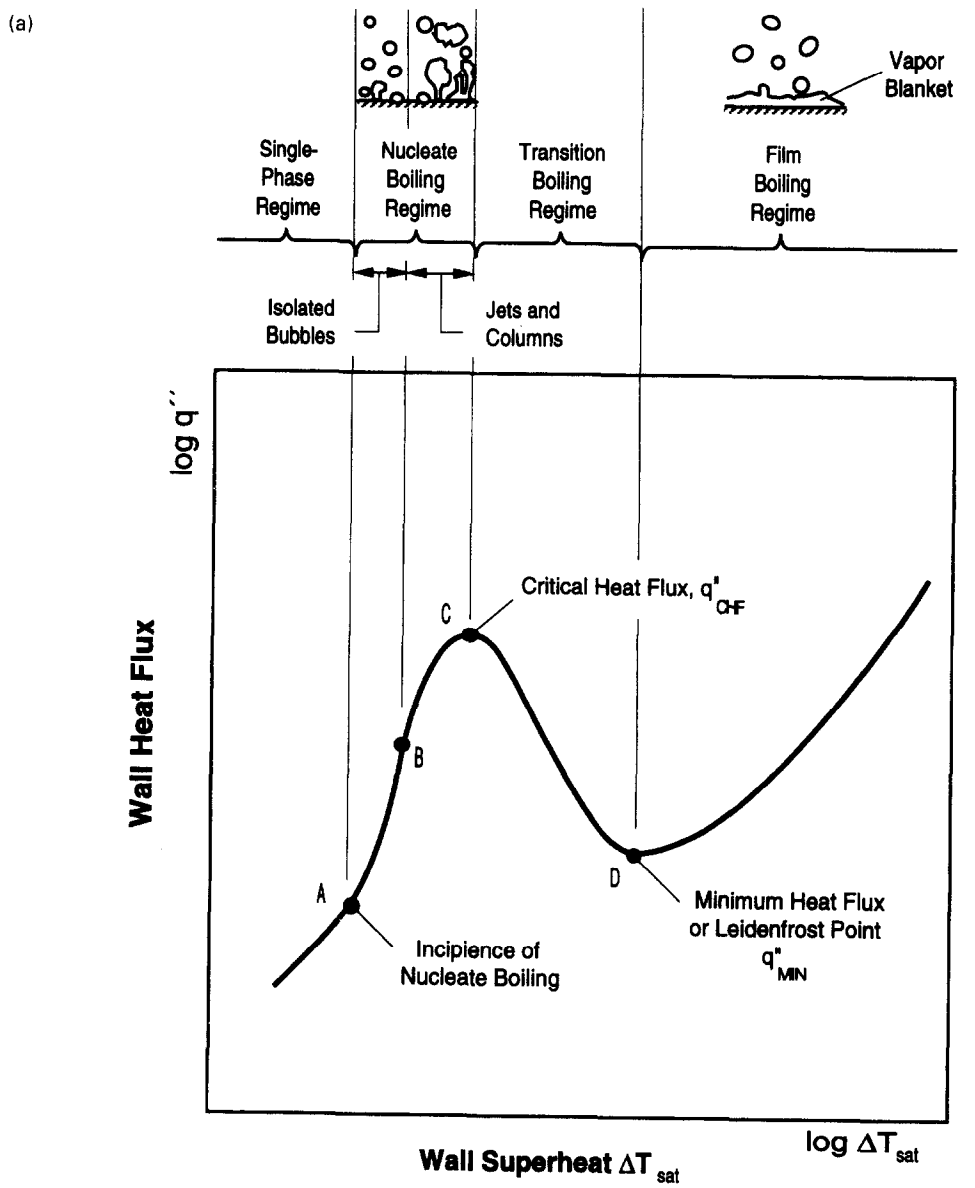

Fig. 1. (a) Boiling curve and (b) corresponding cooling curve for a small solid object in a stagnant bath of liquid. (*Continued overleaf.*)

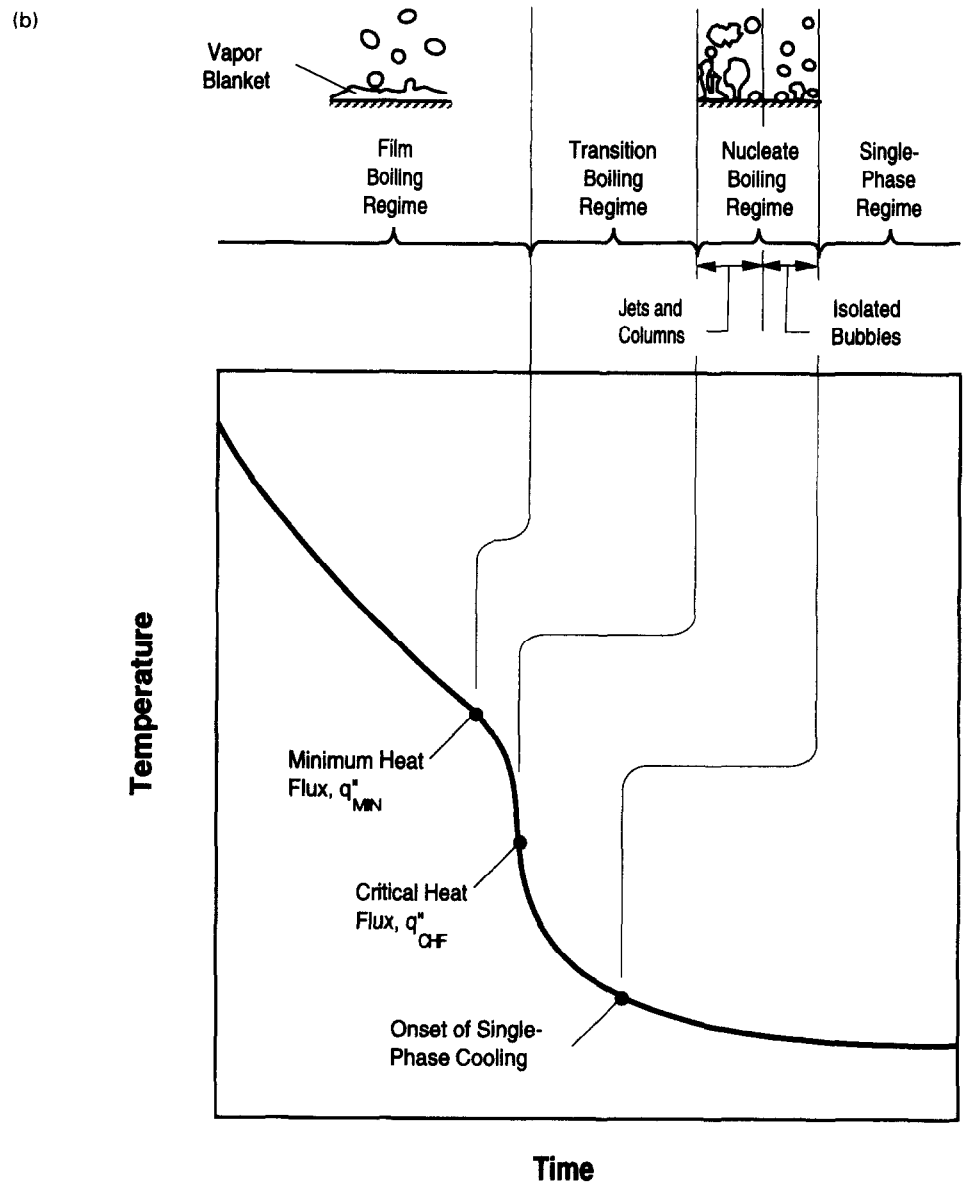

Fig. 1—*Continued.*

approaches were presented in refs. [3, 4] to predict the thickness of the vapor layer separating a hemispherical liquid droplet from a hot surface during film boiling. Gorton [5] found experimentally that, in film boiling, the vapor film thickness between a sessile droplet and the surface increases and the heat transfer coefficient decreases with an increase in surface temperature. Guided by a theoretical analysis, Baumeister *et al.* [6] developed a dimensionless correlation for the vaporization times of discrete liquid masses in the film boiling regime. These four studies are fundamental in nature and lay groundwork which may help in modeling spray heat transfer once the effects of impact velocity and droplet frequency are better understood.

Experimental research on the impact and deformation behavior of a liquid droplet impinging upon a heated surface has relied heavily on high speed photography. In one of the most widely cited studies on droplet impact, Wachters and Westerling [7] observed that the impact and breakup of water droplets striking a 400°C horizontal surface (corresponding to the film boiling regime) could be grouped into three general categories depending upon the droplet Weber number, *We*, which is defined as the ratio of droplet inertia forces to surface tension forces.

$$We = \frac{\rho_f u_o^2 d_o}{\sigma}. \tag{1}$$

In the low Weber number regime, $We \leqslant 30$, the droplet was observed to spread out radially upon impact into a flat disk with a fairly uniform thickness. After extending itself fully, the liquid regrouped under the action of surface tension forces into a globule

which rebounded off the heated surface. In the mid Weber number regime, $30 < We < 80$, the droplet underwent similar behavior as the lower Weber number case except that, upon shrinking and rebounding, the droplet split into a large globule and a small spherical satellite droplet. Finally, in the high Weber number regime, $We \geqslant 80$, upon impact, the droplet began to spread out radially into a flat disk, the rim of which broke into several small droplets which quickly dispersed away from the rim. The flat disk itself then broke up violently into many small droplets.

These observations were confirmed later by Bolle and Moureau [8] who employed high-speed film-based photography (7000 frames s^{-1}) to investigate droplet impact for surface temperatures in the range of 800–1200°C (film boiling regime) and We of 1–1500. Akao *et al.* [9] also performed photographic studies to determine the deformation behavior of water, ethanol, and acetic acid droplets impacting a horizontal surface at 400°C. These droplets also appeared to fit into the three general Weber number categories identified by Wachters and Westerling [7]. The maximum radius of the radially flowing thin film, the residence time of the droplet on the surface, and the heat transmitting area integrated over the residence time were all correlated by Akao *et al.* with respect to Weber number.

Observations by Savic and Boult [10] and Toda [11] indicate for droplets with $We \geqslant 80$ impacting a cold plate ($t_s = 20$°C), the rim of the spreading film follows the surface before breaking up. Engel [12] investigated the impact of water droplets on a glass surface at room temperature using both high-speed photography and Schlieren photographic techniques. In addition, chemical tracing techniques were used to show how, during impact, the droplet spreads out into a thin film composed of radial arms which increase in number with increasing drop size and velocity. Engel observed the rim of the spreading film was thicker than the inner portion of the film and surface roughening promoted droplet breakup. She presented a relation for film spreading radius as a function of time for all times after the droplet dome had disappeared until the time maximum spreading had been reached.

Kurokawa and Toda [13] observed the impact of single droplets onto a glass surface at room temperature using water, ethyl alcohol and mercury for Weber numbers ranging from 150 to 750. The typical behavior of the impacting droplets was similar to that reported by Bolle and Moureau [8]. They also employed a numerical scheme for moving boundary problems to solve the governing continuity and momentum equations. Their numerical predictions of film radius vs time compared fairly well with their experimental data.

In a recent fairly comprehensive photographic study, Chandra and Avedisian [14] investigated the influence of surface temperature on droplet impact dynamics. Using flash photography, they observed the liquid film spreading structure and spreading rate, vapor bubble formation, and contact angle for n-heptane droplets with $We = 43$ impinging upon a polished stainless steel surface. They determined all these impact characteristics were highly temperature dependent over the range of 24–250°C.

Contact areas and the film radius time dependence are crucial to modeling droplet heat transfer. In addition, periods of the various stages of the impact must be known. Akao *et al.* [9] presented a film boiling regime correlation for the droplet residence time, defined as the time elapsed between the droplet's attainment of and detachment from the surface. Wachters and Westerling used the first order period of a freely oscillating droplet to describe the residence time. Akao *et al.* and Senda *et al.* [15] found this relation did not hold well under experimental conditions. Senda *et al.* showed graphically the experimental residence time for water droplets impinging a heated surface ($150 \leqslant T_s \leqslant 400$°C) is about half of the first-order period of a freely oscillating droplet.

Makino and Michiyoshi [16] also investigated the contact period of water droplets. For low velocity water droplets (0.3 m s^{-1}) with a diameter of 2.54–4.50 mm and surface temperatures from 150 to 360°C, they found that, initially, the droplet spreads out into a thin film before boiling. Because of the low droplet velocity used in their study, little or no breakup occurred, which allowed them to develop simple models. Using high-speed photography, they measured and correlated both the contact period, defined as the time from droplet impact to departure from the surface, and the waiting period, the time from impact until boiling incipience.

Several of the correlations and models for the droplet spreading characteristics discussed above are outlined in Table 1. The parametric ranges of the key variables along with the types of liquids and solid surfaces used are also given. In a later section, these correlations and models will be assessed relative to the experimental results of the present study.

Closure modeling of sprays

It is apparent from the above literature review that droplet impact and heat transfer are controlled by several parameters including droplet velocity, droplet diameter and surface temperature. Several investigations have identified droplet Weber number dependent stability regimes, albeit only for the film boiling regime. In addition, empirical correlations have been developed to predict the time dependent spreading area of impinging droplets. While these studies have provided insightful fundamental results, they do not yet constitute a comprehensive basis for a closure spray model. To lay the groundwork for such a model, the following important steps must be accomplished.

(1) There is a need for comprehensive photographic records of droplet impact behavior corresponding to wide ranges of the variables which have been identified by previous investigators for cat-

Table 1. Correlations for spreading characteristics of impinging droplets

Reference	Parameters	Correlations	Notes
Bolle and Moureau [8]		Spreading film radius: $\frac{R}{r_o} = 1.67(3.1\tau - \tau^2)$ Dimensionless time: $\tau = \frac{t}{t^+} = t\frac{u_o}{d_o}$	• Theoretical model • Valid for film boiling • Valid for $0.2t^+ \leqslant t \leqslant (1.20\text{–}1.50)t^+$
Akao *et al.* [9]	$2.1 \leqslant d_o \leqslant 2.9$ mm $0.66 \leqslant u_o \leqslant 3.21$ m s^{-1} $T_s = 400$°C	Maximum spreading radius of film underside: $\frac{R_{max}}{r_0} = 0.613We^{0.39}$	• Experimental correlation • Fluid: water, ethanol, and acetic acid • Surface: copper
Takeuchi *et al.* [17]	$0.02 \leqslant d_o \leqslant 0.60$ mm $2 \leqslant u_o \leqslant 25$ m s^{-1} $200 \leqslant T_s \leqslant 400$°C	Time corresponding to maximum extent of film spread: $t_{max} = -\left(\frac{1}{\sqrt{3}}\right)\ln\left\{\frac{1-\sqrt{\frac{\phi_c^*+1}{3}}}{(2-\sqrt{3})\left(3-\sqrt{\frac{\phi_c^*+1}{3}}\right)}\right\}\frac{d_o}{u_o}$ Non-dimensional height of drop/film: $\phi_c^* = 0.5\cdot\left\{b + \frac{We^{0.56}}{a} - \sqrt{\left(\frac{1}{a}\right)^2 We^{1.12} + \left(\frac{2b}{a} - \frac{8}{a}\right)We^{0.56} + b^2}\right\}$	• Experimental correlation • Fluid: water • Surface: chrome-plated copper • Constants T_s (°C) a b 400 1.442 2.43 300 1.282 2.45 250 1.150 2.56 200 1.557 2.53
Makino and Michiyoshi [16]	$2.54 \leqslant d_o \leqslant 4.50$ mm $u_o \approx 0.3$ m s^{-1} $150 \leqslant T_s \leqslant 360$°C	Contact period (for transition and film boiling): $\tau_c = 1.51\times10^{17}\left(\frac{\rho_s c_{p,s} k_s}{\pi}\right)^{-1.10}\cdot d_o^{1.5}\Delta T_{sat}^{-3.01}$ (s) Waiting or boiling incipience period: $\tau_i = 4.67\times10^{12}\left(\frac{\rho_s c_{p,s} k_s}{\pi}\right)^{-1.07}\cdot\Delta T_{sat}^{-3.35}$ (s) Contact radius of film: $R = 3.16\times10^{-2.0}\cdot t^{0.5}$ (m) $\quad 0 \leqslant t \leqslant \tau_i$	• Experimental correlation • Fluid: water • Drop impact velocity not given but determined from knowledge of syringe to surface height given in photograph • Surfaces: copper, brass, carbon steel, stainless steel •Estimated We range: $3.1 \leqslant We \leqslant 5.6$
Kurokawa and Toda [13]	$150 \leqslant We \leqslant 750$ $850 \leqslant Re \leqslant 50\,000$ $T_s = 22$°C	Maximum film spreading radius: $\frac{R_{max}}{r_o} = 0.96\,Re^{0.095}\,We^{0.084}$	• Experimental and numerical study • Fluid: water, ethyl alcohol and mercury • Surface: glass • $Re = \frac{\rho_f u_o d_o}{\mu_f}$

Units in correlations: $[T]$ = °C, $[d_o, r_o]$ = m, $[u_o]$ = m s^{-1}, $[\rho]$ = kg m^{-3}, $[c_p]$ = J kg^{-1} K^{-1}, $[k]$ = W m^{-1} K^{-1} $[\mu]$ = N s^{-1} m^{-2}, $[t]$ = s.

egorizing droplet regimes; namely, Weber number and surface temperature. These records should cover the low, mid and high Weber number regimes identified by Wachters and Westerling and for temperatures corresponding to all of the boiling regimes, not only film boiling or adiabatic impact.

(2) The photographic records should be converted into impact regime maps which depict transitions in the heat transfer mechanisms occurring during the lifetime of the impinging droplet at every Weber number and in every boiling regime.

(3) From the photographic records, plots depicting the history of liquid spread following impact should be generated. These plots enable the determination of the portion of the surface area undergoing cooling at every instant following the impact.

(4) The above work should be repeated for a stream of droplets in order to ascertain the effects of droplet frequency on heat transfer.

(5) Step 4 above should be repeated for a number of droplet streams impacting simultaneously different portions of the surface to simulate a spray.

The primary objective of this study is to develop a

general understanding of the physical mechanisms of droplet impact and to display results in an informative and compact manner. The above five steps are precisely the framework for this study. Excepting the last step (the focus of future studies), still and high-speed video photography are employed to accomplish the above steps by generating detailed impact regime maps which can be employed by future researchers for the purpose of both obtaining a consolidated understanding of impact behavior and assessing theoretical models describing specific features of the impact. In addition, heat transfer measurements of water droplets impinging on a small preheated disk are used to measure the surface temperatures corresponding to CHF and the LFP for different Weber numbers and surface temperatures.

2. EXPERIMENTAL APPARATUS AND PROCEDURE

The apparatus shown in Fig. 2a was constructed to record the impact behavior of a single droplet or a droplet stream on a hot surface. The apparatus consisted of a fluid delivery system, an impact module, a droplet detector, a stroboscope and a still camera.

The fluid delivery system consisted of a reservoir, a magnetically driven centrifugal pump, stainless steel and Tygon tubing, stainless steel fittings, and a needle valve. The droplets were formed by free fall from a 0.58 mm (0.023 in) diameter hypodermic needle connected to the outlet of the needle valve. The working fluid, deionized water, was replaced frequently to avoid any significant changes to properties due to contamination.

Two droplets impact modules were employed. The first was used in photographic studies of a single droplet impacting a constant temperature surface, and the second in transient heat transfer experiments involving quenching of a surface by a stream of droplets.

Photographic methods

Figure 2a depicts the impact module employed in the photographic study of single droplet impact. This module was fabricated from aluminum and mounted in an insulating housing made from G-7, a fibreglass plastic capable of withstanding surface temperatures exceeding 300°C for short durations. The impact surface was carefully polished; subsequent surface analysis using a profilometer showed its arithmetic average roughness was about 100 nm. Heat was generated by a cartridge heater embedded in the aluminum block, and a chromel–alumel (type K) thermocouple located just beneath the impact surface was used to monitor the surface temperature. A temperature controller was used to manipulate the power input to the cartridge heater in order to maintain the desired surface temperature. The entire heater assembly was mounted on a micrometer translation platform to fine tune the instant of impact associated with the detector circuit as described below.

The entire history of a droplet impact on a surface can be as short as a few milliseconds. To capture events occurring within such a short interval, a Kodak Ektapro 1000 video motion analyzer, capable of speeds up to 1000 full frames per second and 6000 partial frames per second, was used in conjunction with a 200 mm zoom lens and a high intensity light source. While this motion analyzer provided vital information concerning such details of the impact as film spreading, vapor production, and droplet breakup, the resolution of the individual video frames was limited.

To capture crucial instances of the impact with high resolution, a 35 mm camera equipped with bellows and a 200 mm zoom lens was employed. Sharp and high contrast photos were possible by using a high resolution film, Kodak P3200, and a high intensity, short pulse flash from a General Radio Strobotac 1538-A stroboscope. The key to capturing a sequence of photos depicting the crucial stages of impact was timing of the flash to coincide with a given instant of the impact. A droplet detection technique similar in principle to one used by Chandra and Avedesian [18] was utilized to trigger the flash.

The detector mechanism was composed of a He–Ne laser and a dark-activated detector circuit illustrated in Fig. 2b. The operation of the detector was as follows. As the droplet fell from the hypodermic needle and passed through the laser beam, the laser light was scattered and prevented from reaching a photoresistor in the detector circuit. The lack of illumination greatly increased the photoresistor's resistance which caused an optical switch to trip a second circuit, sending a 1 V trigger pulse to a signal generator. Once this occurred, the signal generator delivered a 1V peak-to-peak square pulse to the stroboscope, which fired a short duration flash on the downside of the square pulse. The time delay from the instant the droplet passed through the laser beam to the time the stroboscope fired was controlled by varying the width of the square pulse from the signal generator. The time constants associated with the photoresistor, diodes, and optical switch were several orders of magnitude smaller than the delay time and thus did not have to be accounted for in setting the delay. The reference delay time corresponding to the commencement of droplet impact was set by trial and error. The different subsequent stages of impact were captured by increasing the time delay from the signal generator and by moving the impact surface vertically in small increments with the aid of the micrometer translation platform shown in Fig. 2a.

A consistent procedure was followed in obtaining photographic sequences of single droplet impact except for variations in droplet velocity and surface temperature. First, the high speed video system was used to record several droplet impacts at 20°C surface temperature decrements from 280 down to 100°C and Weber numbers of 20, 60 and 220. These Weber numbers correspond to droplet velocities of 0.70, 1.21 and

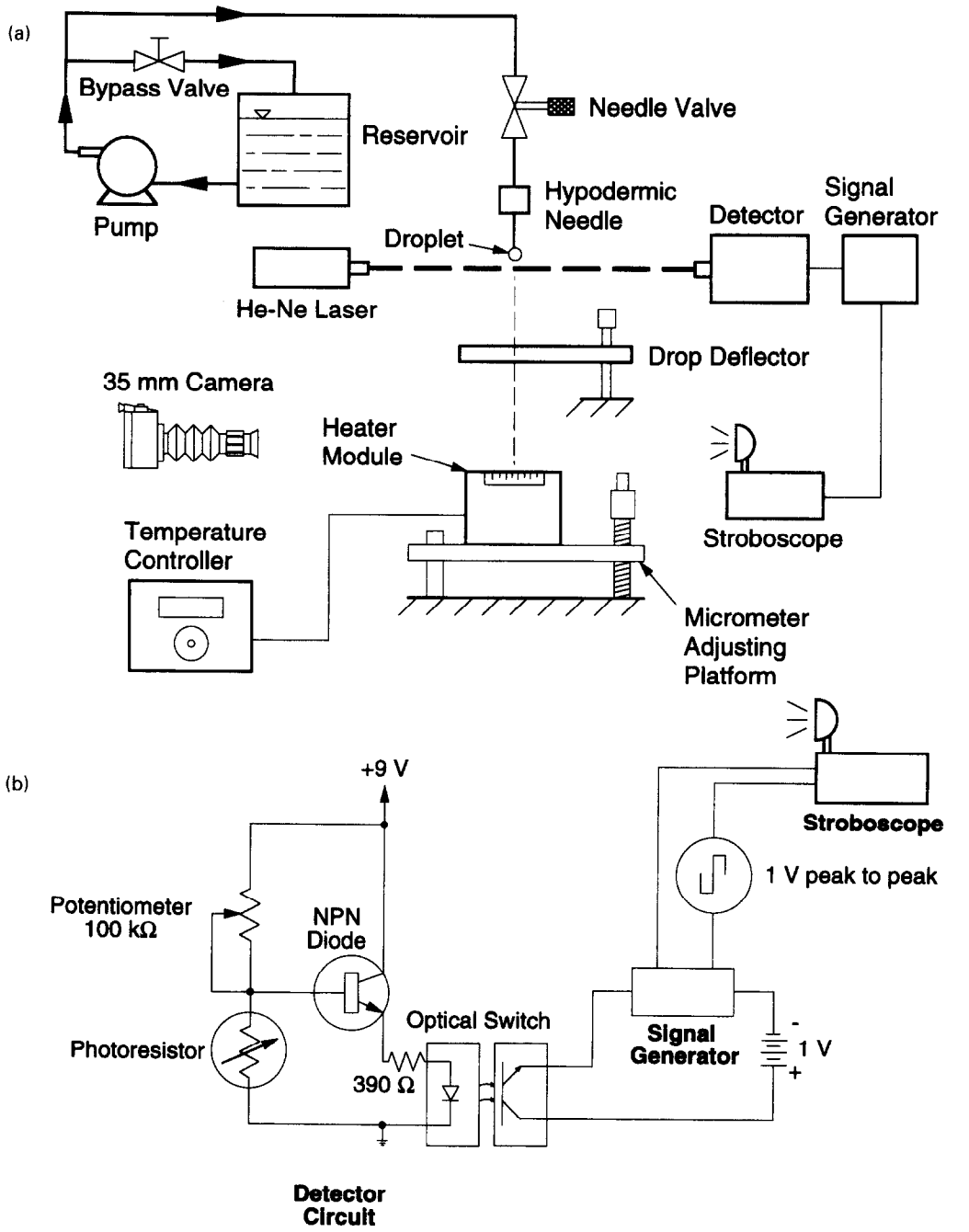

Fig. 2. Schematics of (a) test apparatus and (b) droplet detector and stroboscope trigger circuitry.

2.34 m s^{-1}, respectively, and a fairly constant droplet diameter of about 3.0 mm. The droplet diameter and velocity were determined from a static force balance between gravity and surface tension and free fall kinetics, respectively. These values were then verified with the Ektapro motion analyzer to within 10%.

Upon completing the high-speed video segments, the 35 mm camera was used in conjunction with the detector mechanism to obtain high resolution still photos of several stages of the impact for each of the three Weber numbers and surface temperatures of 125, 180 and 280°C. The still photos were obtained in a dark laboratory because the camera shutter was open several seconds prior to the impact and the corresponding strobe pulse. Following the triggering of the strobe flash, the shutter was closed and the film advanced. Several photographs were taken for a single set of operating conditions before adjusting the time delay to capture a later stage of the impact. The separate impact photos obtained with the 35 mm camera were later pieced together to construct a complete history of the impact and verified with the high-speed video segments. Key to acquiring a meaningful photographic sequence of the impact was to ensure repeat-

ability in droplet generation since each photo in an individual sequence was taken of a different droplet.

Heat transfer measurements

The second impact module, shown in Fig. 3, was composed of a thin gold-plated copper disk mounted in a larger G-7 insulating disk. The copper disk was made thin enough to ensure isothermal conditions throughout the disk at every instant during the quench, and its diameter was chosen to be slightly larger than the maximum spreading diameter achieved by the impinging droplets. The disk was preheated by a 650°C air stream supplied from a heat gun.

The disk temperature was measured by a type K thermocouple bonded to the disk underside. For the thermocouple type, size and bonding method used in the present study, a time constant, defined as the time required for the center of the thermocouple bead to reach 63.2% of an instantaneous change in the temperature of the disk, was estimated at 1.95 ms. Since the largest temperature response of the disk in the present study was about 50°C s^{-1}, it is estimated that the thermocouple response (based on four time constants) would lag the true disk temperature by only 0.39°C.

The heat transfer measurements commenced by setting the needle-to-surface distance and the droplet frequency. A deflector mechanism shown in Fig. 2a was positioned to prevent the droplets from striking the surface prior to heat-up. The copper disk temperature was raised with the aid of the heat gun and monitored by a computer-driven Keithley 500 data acquisition system. Upon reaching a temperature of 280°C, the droplet deflector was removed and the data acquisition program initiated. The transient temperature data were recorded every 20 ms until the disk temperature fell below 100°C. A computer code was used to convert the recorded temperature-time cooling curve similar to the one shown in Fig. 1b to a boiling curve, Fig. 1a, assuming the disk behaves as a lumped mass, from which the temperatures corresponding to CHF and the LFP were determined. This procedure was repeated for droplet Weber numbers of 20, 60 and 220, and frequencies of 40, 75 and 150 droplets per minute (dpm). To insure reproducibility, six tests were conducted for each set of experimental conditions.

This transient technique was adopted because of its simplicity and relatively short measurement duration as compared to steady state methods; both methods are known to produce the same CHF temperature [19, 20].

3. EXPERIMENTAL RESULTS AND DISCUSSION

The experimental results are presented in three sections. First, the droplet impact regime maps and corresponding photo sequences are presented along with experimental measurements of the time-dependent spreading of the liquid film. Next, heat transfer measurements are presented to show the heat transfer characteristics associated with the individual boiling regimes and determine the boundary temperatures between these regimes. Finally, the film spreading data are used to assess several of the models and correlations discussed earlier in the literature review.

Impact regime maps and droplet spreading characteristics

Three Weber numbers, 20, 60 and 220, were used to categorize the impact behavior of individual water droplets. The impact is described in three different ways: (1) impact regime temperature-time maps, (2) time records of droplet spreading radius, and (3) representative photo sequences of the impact.

Each impact regime map, corresponding to a particular droplet Weber number, presents detailed information concerning impact history and the associated fluid and heat transfer interactions as observed using the high-speed motion analyzer. Figure 4 provides details on how to read such a map using a droplet Weber number of 20 as an example. At a given surface temperature (ordinate), the history of the impact and associated heat transfer mechanisms is described by

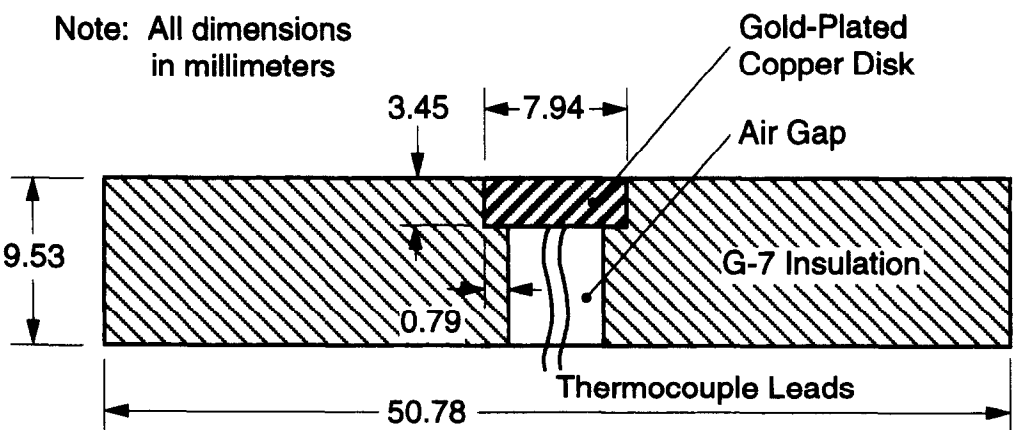

Fig. 3. Construction of droplet impact module used in heat transfer measurements.

following a horizontal line across the regime map corresponding to the lifetime of the impinging drop. At various times along this line, two types of symbols are used to describe the impact: (1) small solid circles describing the impact behavior such as durations of film spread, liquid rebound, and/or complete droplet breakup; and (2) several additional symbols listed in the map legend which describe transitions in the heat transfer mechanisms. For instance, at a surface temperature of 280°C, the maximum extent of the spreading film and the rebound of the droplet are identified by small solid circles. The extent of liquid–solid interaction, defined as a condition of liquid contact with the solid surface during the initial stage of the impact, is represented by an open circle. This interaction extends until sufficient vapor is produced to prevent further liquid–solid contact. For a surface temperature of 130°C, the impact characteristics are quite different from those at 280°C, as noted by a different arrangement of symbols and drastic differences in the total droplet lifetime.

The spatial extent of the spreading droplet, which is not evident in the regime maps, is presented in an accompanying plot of film radius vs time from the instant of impact. The information used to construct both the regime maps and droplet spreading plots was obtained from high-speed video footage, which is also represented by the still photo sequences. The liquid–solid interaction periods around and above the LFP (noted in the impact regime maps) were substantiated by the use of an electrical circuit and storage oscilloscope described in ref. [1]. The oscilloscope readings revealed intermittent liquid–solid contact occurred during most of the droplet spreading time of 3–6 ms, depending on the droplet Weber number. The droplet spreading plots and photo sequences correspond to surface temperatures of 280, 180 and 125°C which fall within the film, transition and nucleate boiling regimes, respectively. For the 125°C case, the impact and boiling behavior was very similar for the three Weber numbers, thus only one sequence of still photos, corresponding to a Weber number of 220, is given for this temperature. For the 180 and 280°C cases, photo sequences are presented for each of the three Weber numbers.

Low Weber number results. Figure 5a–5c shows, respectively, the impact regime map, droplet spreading plot, and photo sequences corresponding to a relatively low Weber number of 20 for which surface tension forces play a major role in resisting droplet breakup. Noted in the impact regime map are the dominant characteristics of the droplet during its lifetime for various temperatures. Also noted are the four distinct heat transfer regimes of film boiling, transition boiling, nucleate boiling, and thin film evaporation, as well as the LFP and CHF temperatures determined from the quench experiments described later.

For a surface temperature of 280°C, corresponding to the film boiling regime, Fig. 5a and c shows the droplet spreads into a relatively thick, intact film during the first 4 ms of impact. Electrical contact measurements revealed the liquid film makes some contact with the surface during the first 6 ms, even at this film boiling surface temperature, after which the film becomes separated from the surface by a thin vapor layer. Strong surface tension forces at this low Weber

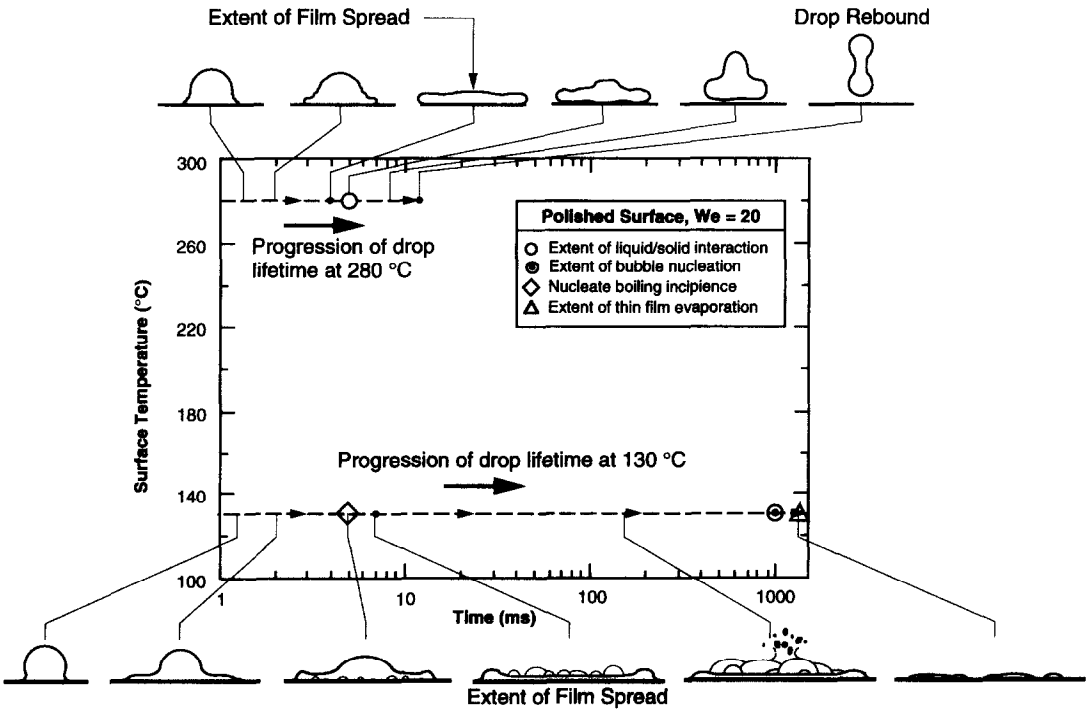

Fig. 4. Schematic aid for reading droplet regime maps.

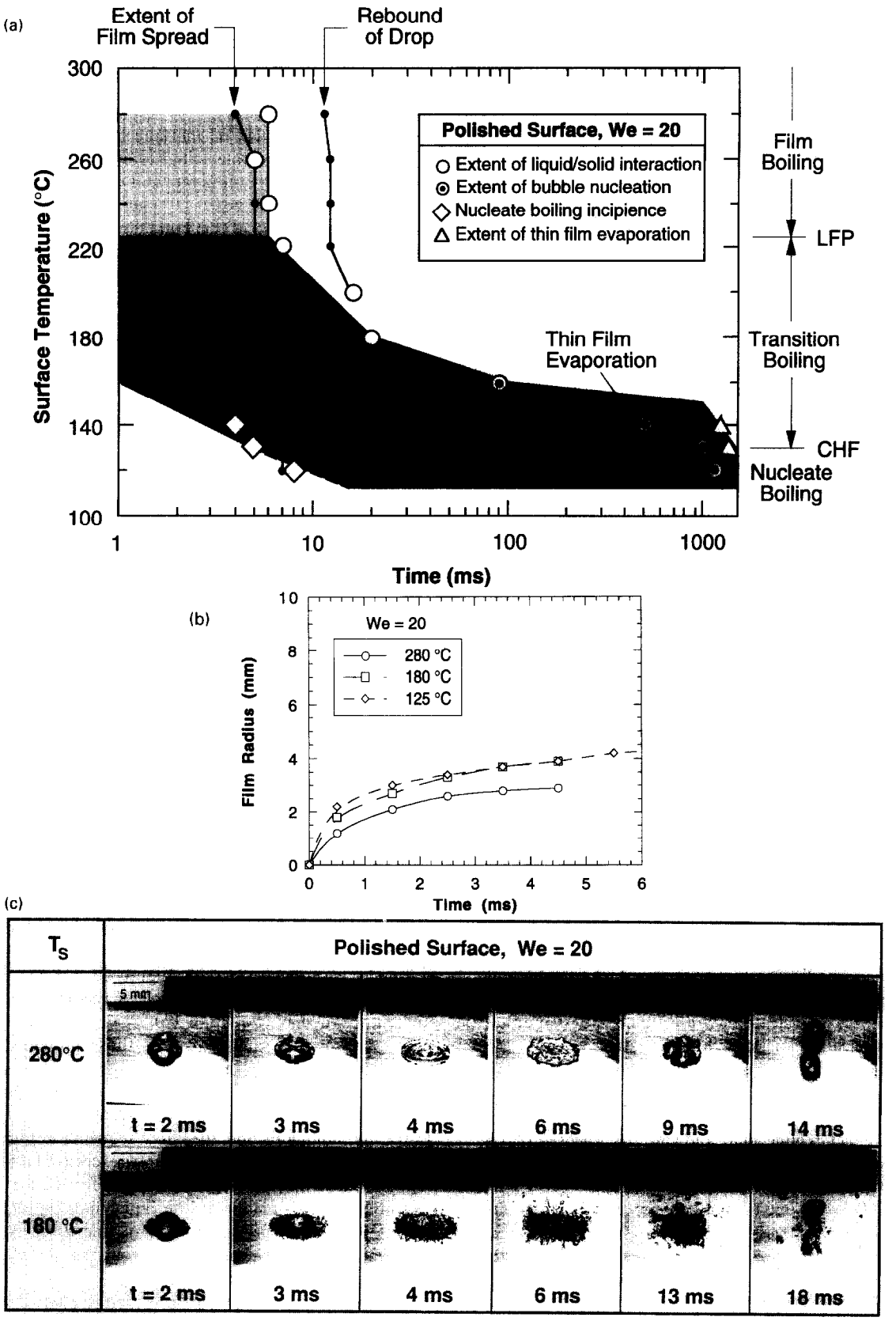

Fig. 5. (a) Droplet regime map, (b) spreading film radius vs time, and (c) photo sequences for $We = 20$.

number cause the liquid to regroup as a distorted droplet which rebounds from the surface over the next 10 ms. This behavior is characteristic of all temperatures in the film boiling regime above the LFP temperature of about 225°C.

The impact behavior for the transition boiling regime varies drastically over the temperature range of 225–130°C. At the high end of this range, the impact behavior is somewhat similar to that of film boiling, however, more extensive liquid–solid contact begins to occur. Near the midpoint of the transition regime, represented by the photo sequence in Fig. 5c corresponding to a surface temperature of 180°C, the liquid film becomes highly disturbed but remains intact for the first 5 ms, after which it begins to break up into several ligaments. Surface tension forces still manage to regroup most of the liquid, but allow small satellite droplets to break free. At temperatures below the LFP, liquid–solid contact decreases the liquid–vapor free surface area and hence weakens the surface tension forces which resist the liquid spread. Figure 5b reveals liquid–solid contact enhances the spreading rate and extent of the liquid film in the transition boiling regime as compared to the film boiling regime. At the lower end of the transition regime, from 160 to 130°C, the droplet lifetime on the surface is greatly extended. During the initial film formation, boiling incipience, observed as vapor bubble formation and represented as a dashed line on the regime map, is delayed several milliseconds. Following incipience, vigorous boiling occurs over a period of up to several hundred milliseconds, followed by thin film evaporation of the remaining liquid up to over a thousand milliseconds.

The nucleate boiling regime exists over a small temperature range from 130–110°C, the higher of which corresponds to the CHF temperature. Figure 5b indicates that for a surface temperature of 125°C, the droplet initially spreads into a thin film at a rate nearly identical to a droplet at 180°C. Upon reaching its maximum radial extent in about 6 ms, the film experiences boiling incipience, followed by vigorous boiling, and finally thin film evaporation. During the final stages of nucleate and transition boiling, vapor bubble nucleation and growth both cease as thin and broken films of liquid begin to dissipate heat by conduction and evaporation.

The droplet impact characteristics shown in the impact regime map and photo sequences of Fig. 5 reveal behavior similar to that reported in Fig. 11 of Chandra and Avedisian [14] for low Weber number ($We = 43$) impact of n-heptane droplets on a polished surface stainless steel surface. The relatively stable impact reported in both studies is to be expected since such low Weber numbers correspond to fairly stable droplets where surface tension forces tend to overcome the breakup effects of inertia and pressure. This consistent behavior supports the generality of the current study since n-heptane has properties considerably different from those of water.

Intermediate Weber number results. The layout for Fig. 6a–c, corresponding to a droplet Weber number of 60, resembles those of Fig. 5a–c. The main differences, which become apparent from the droplet spreading plot and still photo sequences, are the dynamics and stability of the spreading film. For $T_s = 280$°C, the moderate initial momentum of the droplet causes the spreading rate and extent of intact radial film spread to be nearly 50% greater than those for $We = 20$. Breakup of the liquid film is believed to be promoted by liquid ejection and interfacial instabilities caused by the formation of a number of vapor bubbles during liquid–solid contact, as was suggested by Inada and Yang [21] in their study of the breakup of sessile water droplets. These rapidly forming bubbles are ejected up through the spreading liquid film, creating a fine mist of small droplets and a series of larger liquid ligaments as shown in Fig. 6c. At roughly 6 ms after impact, the film breaks up into a number of small droplets which continue to break up upon the surface up to 9 ms after which the finer droplets are completely ejected from the surface.

The transition boiling portion of the map in Fig. 6a is similar in appearance to that presented earlier in Fig. 5a except for the existence of film breakup for $We = 60$. The breakup is depicted in the photo sequence in Fig. 6c corresponding to $T_s = 180$°C. The breakup occurs within several milliseconds of impact producing a spectrum of droplets which are dispersed in every direction. The enhanced boiling and increased momentum of the higher Weber number droplets is believed to be the cause of this violent breakup. In comparing Figs. 5b and 6b, it appears the increased velocity for $We = 60$ enhances both the spreading rate and extent of film spread. The breakup behavior of the liquid film was observed over most of the transition regime, but at the lower temperatures of 160–130°C, a thin evaporating film remained after breakup and dispersion of the fine drops. The nucleate boiling regime was identical to that discussed in reference to Fig. 5a.

High Weber number results. Figure 7a–c display, respectively, the regime map, droplet spreading plot, and photo sequences for $We = 220$. Again, the regime map possesses the same layout as those presented earlier, but as the droplet spreading plots and photos indicate, the impact characteristics are significantly different from those at the two lower Weber numbers. In the film boiling regime, the photo sequence in Fig. 7c corresponding to $T_s = 280$°C shows excessive boiling and instabilities throughout the film for the first few milliseconds of impact. The liquid film rapidly breaks up into a large dispersion of fine droplets, completing the exchange of heat from the surface within only 4 ms after impact.

The transition boiling regime is characterized by increasing droplet impact lifetimes with decreasing surface temperature. At 180°C, the midpoint of the transition regime, the droplet spreads into an unstable film in less than 4 ms, during which vapor is produced

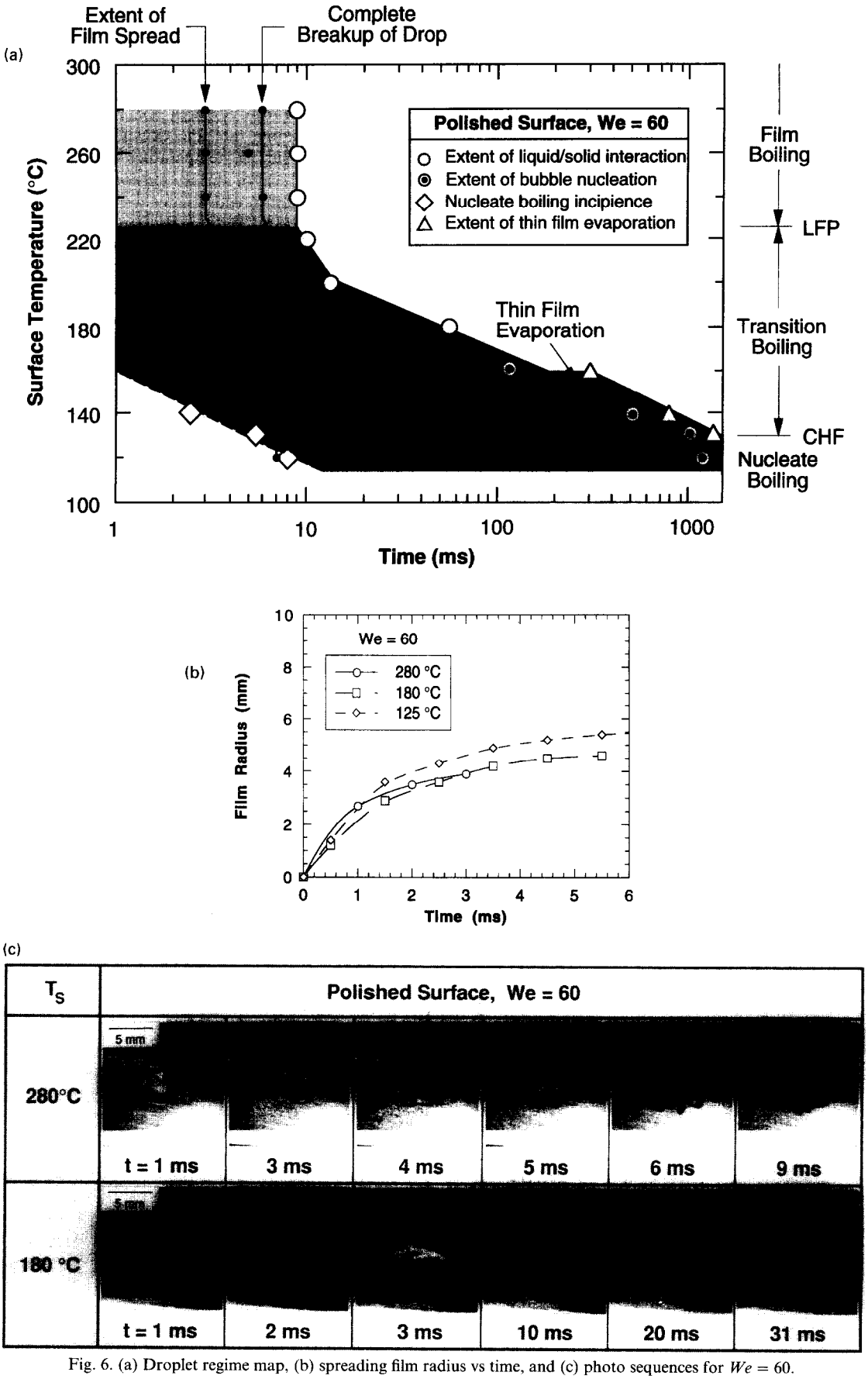

Fig. 6. (a) Droplet regime map, (b) spreading film radius vs time, and (c) photo sequences for $We = 60$.

within the film. This vapor production eventually causes the film to break up into a large array of droplets which spread radially outward. This behavior exists at all temperatures down to CHF. In the temperature range from 180–130°C, boiling incipience is further delayed and thin film evaporation becomes significant with decreasing temperature as indicated in Fig. 7a.

Nucleate boiling exists between 130 and 110°C and is represented in the photo sequence of Fig. 7c corresponding to $T_s = 125$°C. As mentioned earlier, droplet impact behavior in the nucleate boiling regime is similar for all three Weber numbers. The droplet first strikes the surface and spreads into a fairly stable film. Upon reaching its maximum radial extent, bubbles begin to nucleate within the film and burst at the film interface. Gradually, more bubbles form which consume virtually all of the liquid in about 1500 ms. A characteristic difference between the high Weber number droplets and those with lower Weber numbers is the relatively large radial film spread dependence on surface temperature for high *We*. For $We = 220$, the droplet spreading rate and extent both increase with decreasing surface temperature. As suggested earlier, the liquid–vapor surface tension forces which resist the liquid film spread become weaker as surface temperature decreases and more liquid–solid contact occurs. This behavior, observed previously in Fig. 5b for $We = 20$, is even more pronounced in Fig. 7b corresponding to $We = 220$. These data reveal the film spreading rate and extent are dependent on both Weber number and surface temperature.

Several important general observations can be inferred from the regime maps. First, each map por-

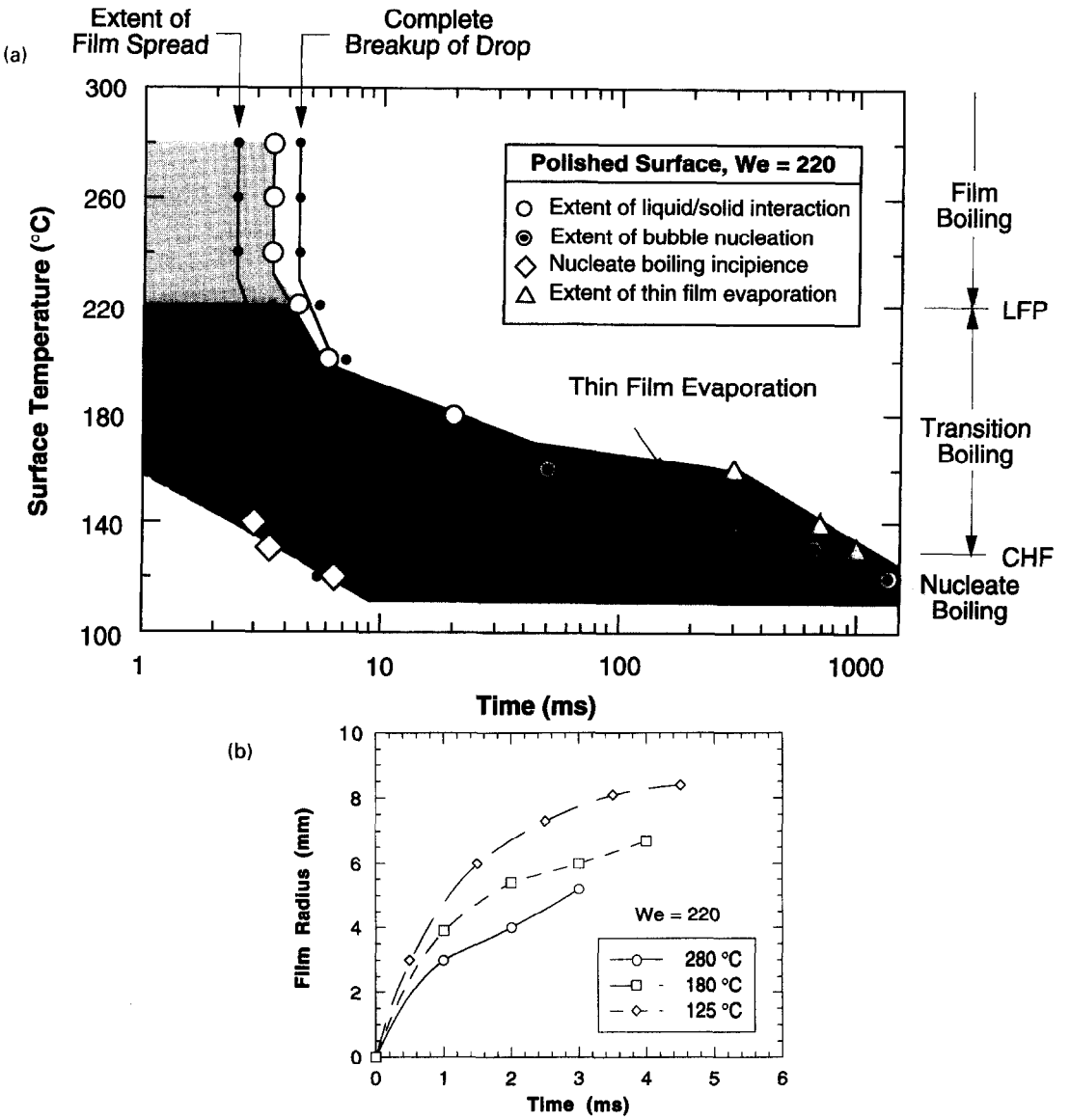

Fig. 7. (a) Droplet regime map, (b) spreading film radius vs time, and (c) photo sequences for $We = 220$.
(*Continued opposite.*)

(c)

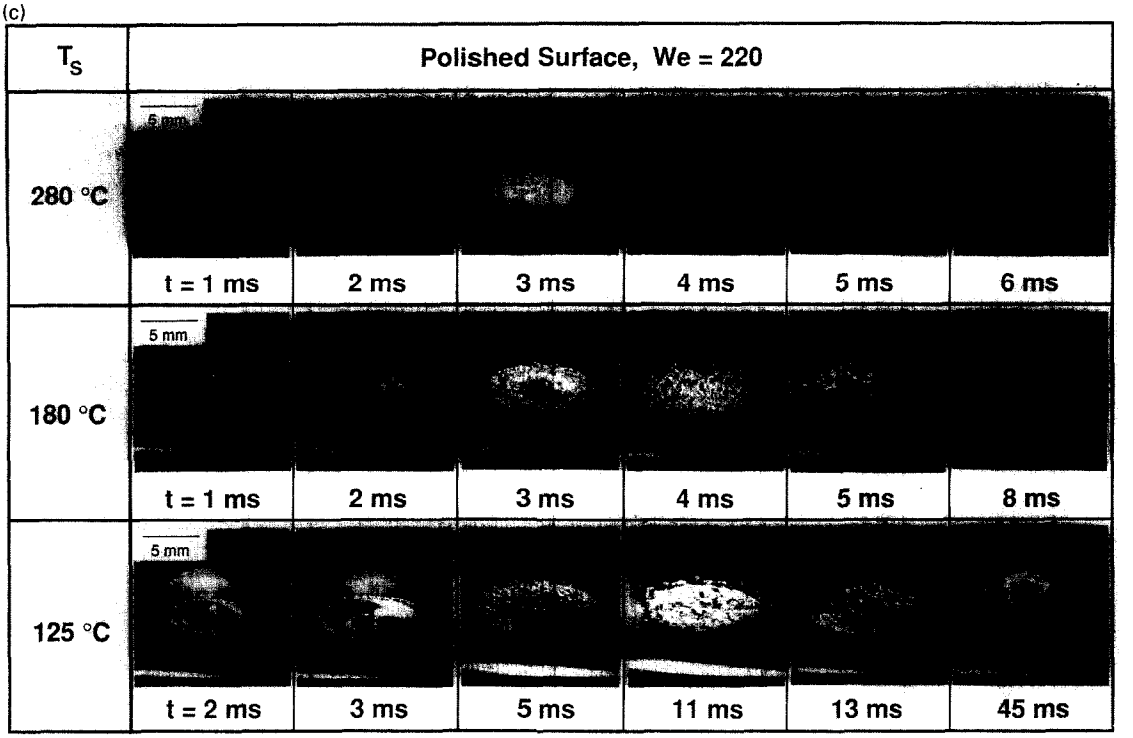

Fig. 7—*Continued.*

trays distinct temperature dependent heat transfer regimes. As will be discussed in the next section, the boundaries to the boiling regimes, CHF and the LPF, are nearly independent of droplet Weber number. On the other hand, the droplet dynamics and corresponding heat transfer mechanisms are characteristically different for each of these regimes. Additionally, the impact characteristics within each regime, such as film stability, spreading rate, and droplet breakup, are highly dependent on droplet Weber number.

Heat transfer measurements

The CHF and LFP boundaries which separate the transition boiling regime from the nucleate and film boiling regimes, respectively, in the impact regime maps were determined from heat transfer measurements of a stream of droplets impacting the small gold-plated copper disk illustrated in Fig. 3. Figures 8–10 show the transient cooling curves and corresponding boiling curves for the three Weber numbers and impingement frequencies of 40, 75 and 150 dpm, respectively. The boiling curves are plotted vs excess surface temperature, $T_s - T_f$, where $T_f = 23°C$. Each of the cooling and boiling curves in Figs. 8–10 is representative of six sets of experimental data obtained for each set of operating conditions.

Periodic jumps which coincide with the arrival of the droplets are apparent in both the cooling curves and corresponding boiling curves. These jumps are most evident in Fig. 8a corresponding to $We = 20$. The horizontal portion of the step corresponds to the slow free convection cooling to the air between droplet impacts, while the sharp vertical portion of the step corresponds to the rapid cooling associated with the impact. This trend is visible in the boiling curve as well, where the dips correspond to the low heat transfer rates between droplet impacts, or the horizontal portions of the steps in the cooling curve. The peaks on the individual jumps in the boiling curves correspond to the rapid cooling associated with the intermittent droplet impact. Since the heat fluxes during impact correspond to large temperature drops, the peaks in the boiling curves are wider than the dips which correspond to the small temperature drops experienced between droplets. Figures 8–10 reveal the periodicities increase in number but damp out in magnitude as the droplet frequency is increased, approaching a smooth continuous curve at 150 dpm. These fluctuations in the boiling curve resulted in a $\pm 10°C$ uncertainty band in the determination of the CHF and the LFP temperatures. It should be noted that, as the disk cooled to 100°C in each experiment, the droplet deflector shown in Fig. 2a was repositioned to deflect the droplet stream. This caused the warmer insulation to reheat the disk slightly, which explains the small increase in the disc temperature toward the end of the quench in Figs. 9a and 10a.

The shape and extent of the boiling curves and, in particular, the small heat flux variation over the surface temperature range corresponding to film boiling are similar to results presented by Senda *et al.* [15] and Pedersen [22] who used much higher droplet frequencies than those employed in the present study. The increase in heat flux in film boiling with increasing droplet velocity is also in agreement with the findings of Pedersen.

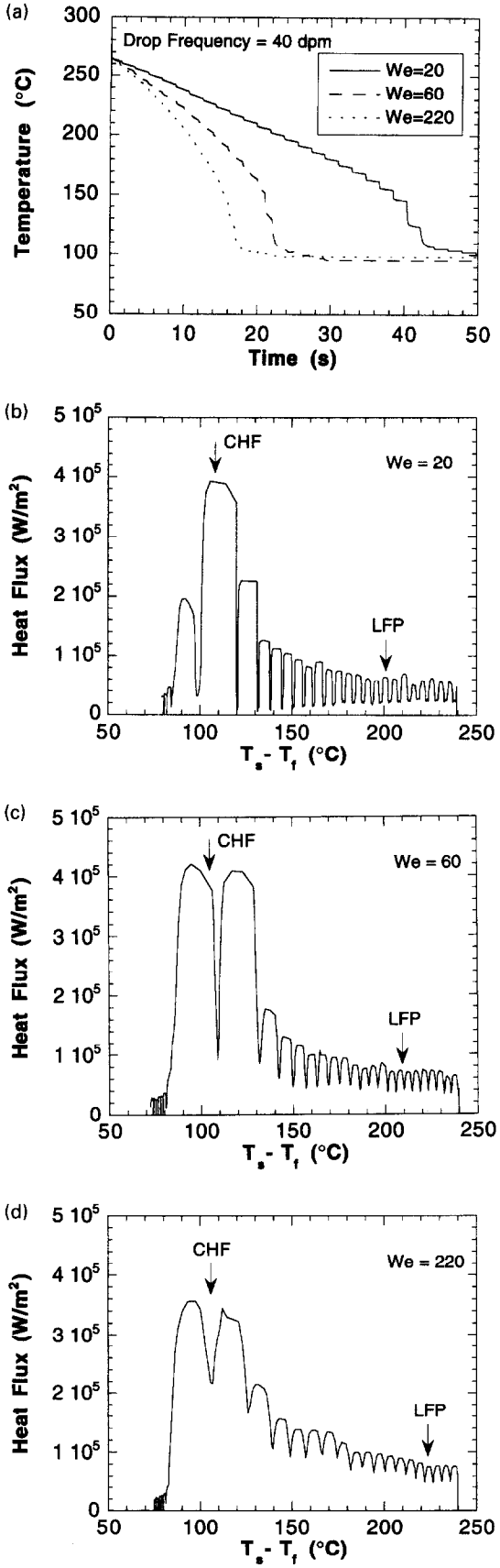

Fig. 8. (a) Cooling curves and corresponding boiling curves for water droplets with Weber numbers of (b) 20, (c) 60, and (d) 220 and frequency of 40 dpm.

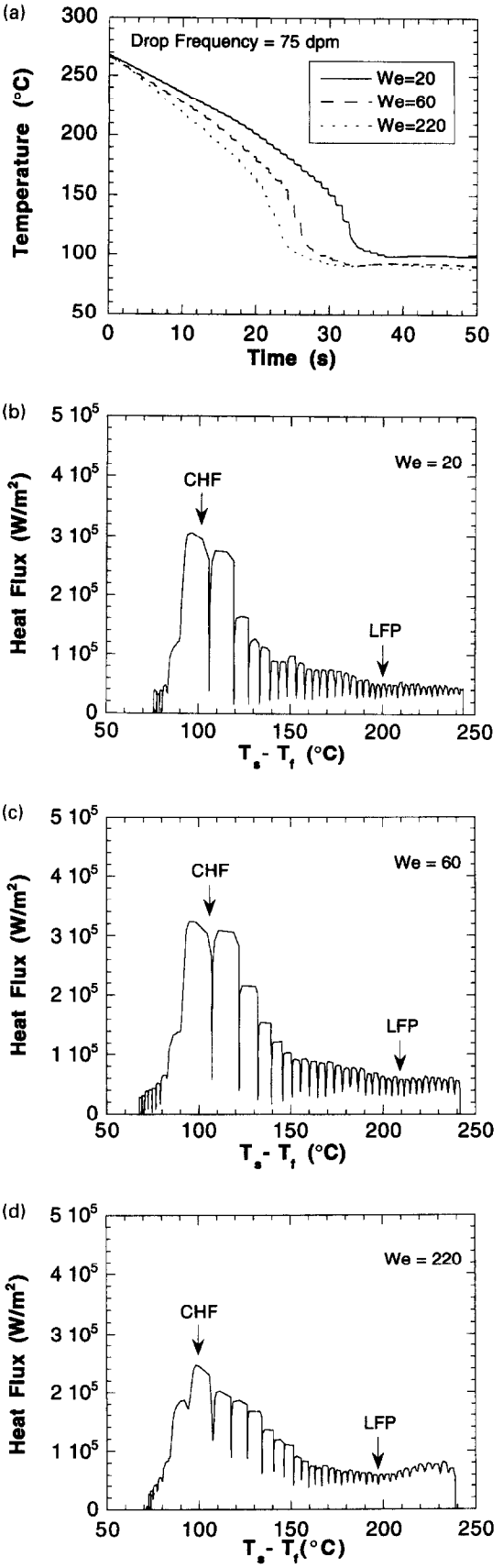

Fig. 9. (a) Cooling curves and corresponding boiling curves for water droplets with Weber numbers of (b) 20, (c) 60, and (d) 220 and frequency of 75 dpm.

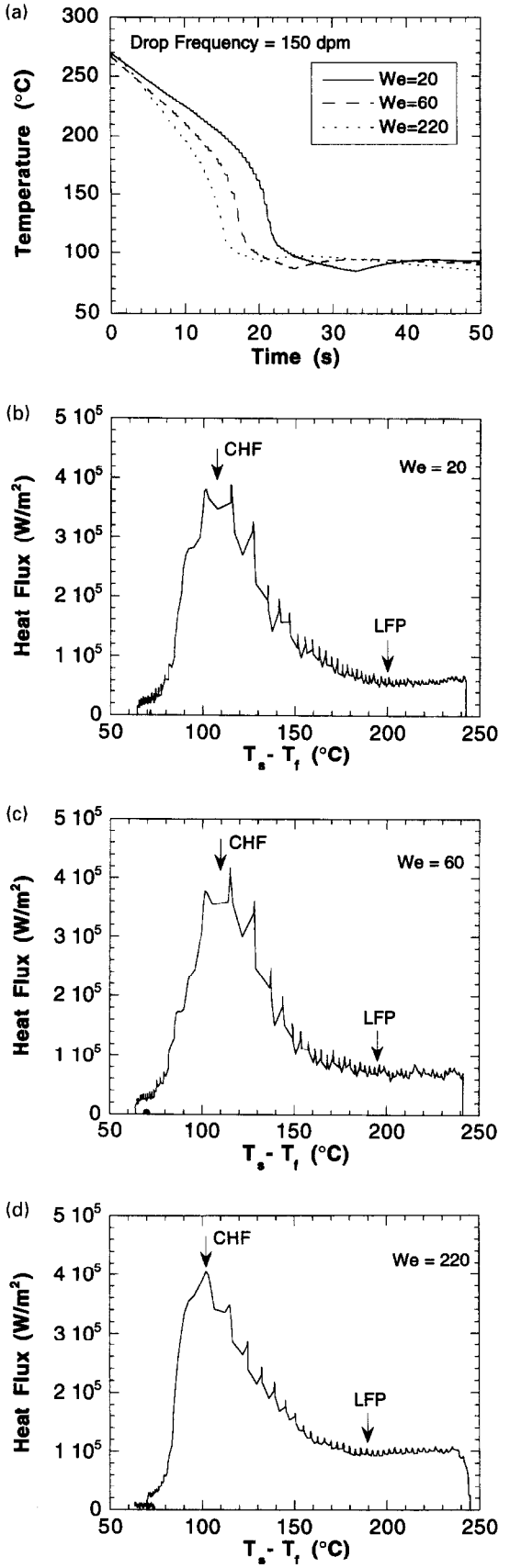

Fig. 10. (a) Cooling curves and corresponding boiling curves for water droplets with Weber numbers of (b) 20, (c) 60, and (d) 220 and frequency of 150 dpm.

The temperatures corresponding to CHF and the LFP, obtained from the boiling curves in Figs. 8–10, are displayed in Fig. 11. While the CHF temperature was easily identified as the point corresponding to maximum heat flux on the boiling curve, the LFP was more difficult to ascertain due to the shallow slope of the film boiling portion of the curve. The LFP temperature was defined as the point at the lower end of the film boiling regime where a sharp rise in heat flux began with decreasing surface-to-liquid temperature difference, $T_s - T_f$. These LFP values are consistently higher than those obtained by the authors in a current study of sessile droplet boiling behavior on similar surfaces. The cause of this difference is speculated to be the result of the higher liquid–solid interfacial pressure which accompanies impinging compared to sessile droplets.

The temperatures given in Fig. 11 are averaged from six experimental runs with error bands of $\pm 10°C$. The two shaded bands in Fig. 11 extend 10°C above the highest temperature and 10°C below the lowest temperature for the respective CHF and LFP data. An unexpected trend that is apparent from the data is CHF and the LFP are relatively insensitive to both droplet impact frequency and velocity. Senda *et al.* [15] and Halvorson *et al.* [20] reported the CHF temperature for water droplets striking a heated surface showed only modest increases with increasing frequency, from 125–145°C and 135–150°C, for frequency increases of 150–900 and 6000–60 000 dpm, respectively. In neither case, however, were the temperature uncertainties reported, but it is difficult to ascertain the CHF temperature from the boiling curves provided by Senda *et al.* with any accuracy better than $\pm 5°C$. Interestingly, Senda *et al.* also reported a CHF temperature of 145°C for sessile droplets, revealing a relative insensitivity of the CHF temperature to droplet velocity. Furthermore, the CHF temperature ranges reported in Refs. [15, 20] correspond closely to those of the present study despite the much higher frequencies used in the two previous studies.

Pedersen [22] suggested the LFP temperature could be influenced by droplet impact velocity and surface roughness, but did not provide any supporting experimental evidence. Senda *et al.* presented experimental data to show that a LFP temperature of 240°C for water droplets impacting a chrome-plated copper surface was independent of droplet frequency. While no temperature uncertainties were provided in their study, it is apparent from their boiling curves estimates of the LFP temperature could be no better than $\pm 10°C$. Senda *et al.* also indicated the LFP temperature for impinging droplets was 10°C greater than that for sessile droplets on an identical surface, suggesting a small influence of droplet velocity on the LFP temperature.

Assessment of models

The dependence of the film spreading characteristics on surface temperature and Weber number is

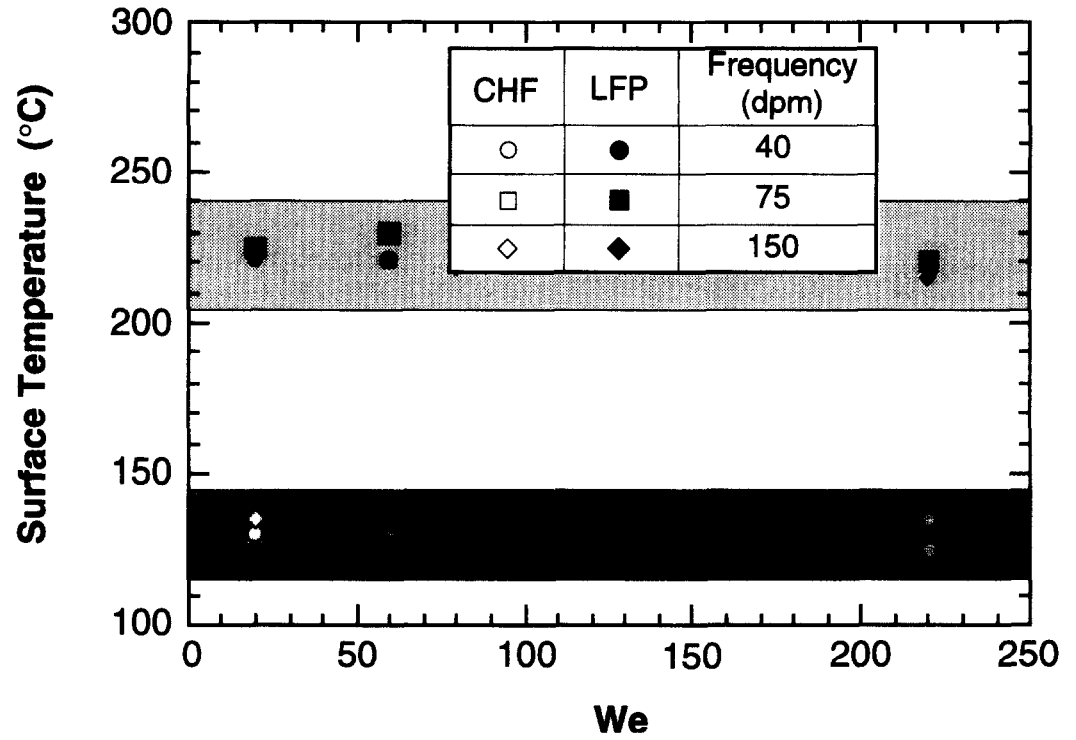

Fig. 11. Surface temperature corresponding to CHF and LFP for different Weber numbers and frequencies.

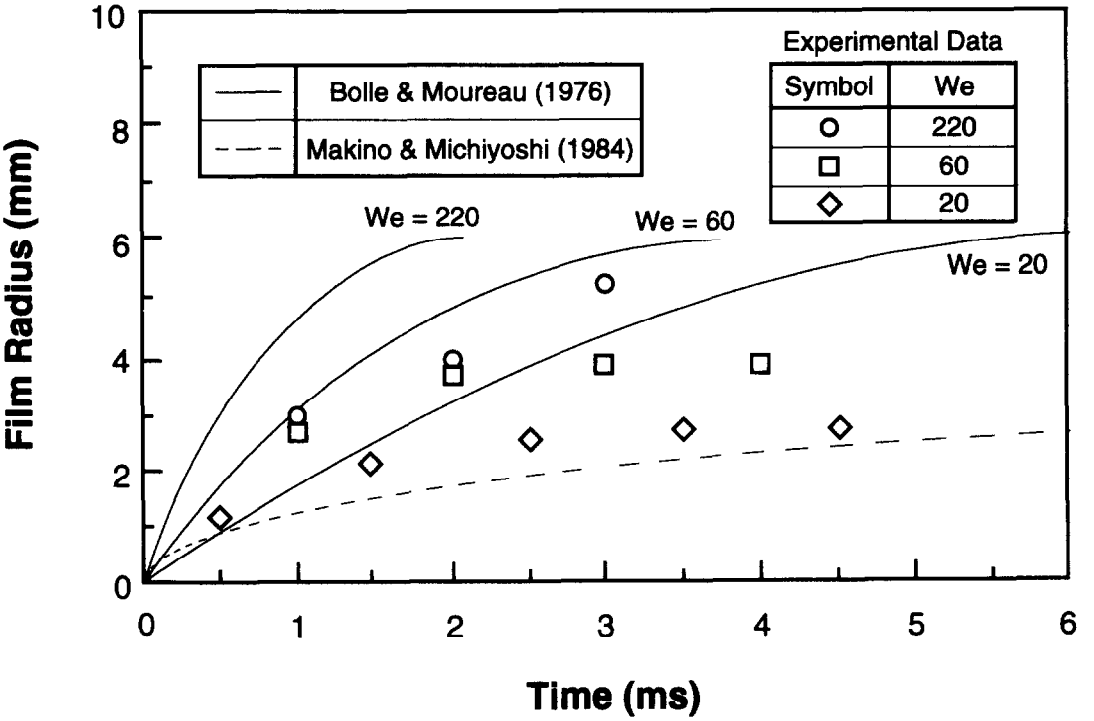

Fig. 12. Comparison of measured liquid film spreading radius with predictions based upon previous models.

clearly evident in the regime maps. However, only a few attempts have been made in the past to completely and accurately account for these variables in film spreading models and correlations. Table 1 gives a representative summary of such efforts. Figure 12 compares the film spreading characteristics predicted according to Bolle and Moureau's model [8] and Makino and Michiyoshi's semi-empirical model [18] for film boiling to the present experimental data given earlier in Figs. 5b, 6b, and 7b. The geometrical model

Table 2. Comparisons of predictions of droplet spreading models and correlations with present experimental data

Reference	We	T_s (°C)	R_{max} (mm)			t_{max} (ms)			τ_c (ms)			τ_i (ms)		
			Pred.	Exp.	% error	Pred.	Exp.	% error	Pred.	Exp.	% error	Pred.	Exp.	% error
Bolle and Moureau [8]	20	280	6.0	2.9	106.9	6.5	4.5	44.4						
	60	280	6.0	4.2	42.9	3.8	4.0	5.0						
	220	280	6.0	5.2	15.4	2.0	3.0	33.3						
Akao *et al.* [9]	20	280*	2.9	2.9	0.0									
	60	280*	4.5	4.2	7.1									
	220	280*	7.5	5.2	44.2									
Takeuchi *et al.* [17]	220†	200				2.6	3.5	25.7						
	220†	250				2.9	3.0	3.3						
Makino and Michiyoshi	20‡	180							34.1	20.0	70.5	2.6	<1.0	>160.0
[16]	20‡	280							3.0	12.0	83.3	0.2	<1.0	>80.0
Kurokawa and Toda [13]	220 ($Re = 7305$)	22	5.3	5.5	3.6									

* The highest surface temperature in the present study of 280°C was used while the correlation was developed for 400°C. This is justified by the relative temperature independence of impact behavior in film boiling.

† Experimental droplet size is outside of range used to develop the semi-empirical model, however, the experimental Weber number of the present study is within the model's range.

‡ The correlation was developed for $3.1 \leqslant We \leqslant 5.6$.

of Bolle and Moureau does not account for fluid properties or surface temperature, which explains the considerable error in predicting the film spreading characteristics. Makino and Michiyoshi's semi-empirical model, which is valid for low velocity water droplets ($3.1 \leqslant We \leqslant 5.6$), shows reasonable agreement with the spreading characteristics for only the lowest Weber number of the present study ($We = 20$), which illustrates the model's weakness in modeling large droplets and high impact velocities.

Table 2 compares several impact parameters predicted according to the models and correlations given in Table 1 with experimental data of this study. The Weber numbers and surface temperatures listed in the table correspond to the present experimental conditions which are within, or as close to as possible to the parametric ranges for the different models and correlations. Special notes are provided for each case where the experimental conditions of the present study fall outside of the recommended parametric ranges of the respective model or correlation. The percent errors for the maximum spreading radius, R_{max}, and corresponding time, t_{max}, range from 0.0 to 106.9% and 3.3 to 44.4%, respectively. Predictions of contact period, τ_c, and incipience time, τ_i, are in considerable error. Good agreements are evident for certain impact parameters, alas only for specific conditions. For example, the R_{max} predictions by Akao *et al.* [9] are in excellent agreement with the present measurements for Weber numbers of 20 and 60, but in poor agreement for $We = 220$. It is apparent from these comparisons there is a need for improvement of accuracy as well as broadening of the parametric ranges of droplet impact studies.

The limitations of the existing models and correlations are a major impetus for developing the impact regime maps presented earlier in this study. Empirical maps have been widely adopted in the two-phase literature to determine, for example, the flow pattern corresponding to different operating conditions. The two-phase flow pattern maps have served both as simple tools for engineering calculations as well as a basis for assessing the validity of theoretical models governing transitions between two-phase flow regimes. The droplet impact regime maps presented in this study were developed to serve a similar purpose. They constitute a convenient guide for identifying important parameters which govern the spreading and breakup of droplets, describing the impact behavior, determining the duration of each mode of liquid–solid interaction during the droplet lifetime, as well as to serve as a basis for assessing the validity of future theoretical or numerical models of droplet impact.

4. CONCLUSIONS

Two types of studies were performed to explore the liquid spreading behavior and heat transfer regimes associated with droplet impact. They included photographic studies of single droplets impacting a hot isothermal surface, and quenching of a small surface by a droplet stream. These studies encompassed three Weber numbers and surface temperatures corresponding to the film, transition, and nucleate boiling regimes of sprays. Key accomplishments from this study are as follows:

(1) Both still and high-speed video photography were used to construct impact regime maps as well as the history of droplet spread. The maps were designed to serve several important purposes including (a) determining the impact behavior of droplets for different surface temperatures and different Weber numbers, (b) ascertaining the important transitions in liquid–solid interaction during the lifetime of a droplet and (c) serving as a basis for assessing the validity of future theoretical or numerical models of droplet impact.

(2) For each Weber number, distinct temperature dependent heat transfer regimes were identified, each possesses different droplet impact characteristics and corresponding heat transfer modes.

(3) Droplet Weber number has a strong influence on the spreading characteristics and integrity of the droplet. In the film boiling regime, strong surface tension forces in low Weber number droplets ($We = 20$) preserve the liquid continuum, causing rebound of the entire droplet following impact. Increasing Weber number in all boiling regimes decreases the spreading time and increases the instabilities responsible for liquid breakup.

(4) The CHF and LFP boundaries determined from the quench experiments are fairly insensitive to both droplet Weber number and frequency over the ranges of the present study.

Studies are ongoing to investigate the effects of surface roughness on impact behavior and to accurately measure the heat transfer rates during droplet impact; work which will further enhance the droplet regime maps of the present study.

REFERENCES

1. J. D. Bernardin, Intelligent heat treatment of aluminum alloys: material, surface roughness, and droplet-surface interaction characteristics. Masters Thesis, Purdue University, West Lafayette, IN (1993).
2. D. D. Hall and I. Mudawar, Predicting the impact of quenching on mechanical properties of complex-shaped aluminum alloy parts, *ASME J. Heat Transfer* **117**, 479–488 (1995).
3. L. H. Wachters, H. Bonne and H. J. Van Nouhuis, The heat transfer from a hot horizontal plate to sessile water drops in the spheroidal state, *Chem. Engng Sci.* **21**, 923–936 (1966).
4. P. B. Whalley, *Boiling, Condensation and Gas-Liquid Flow*. Oxford University Press, New York (1987).
5. C. W. Gorton, Heat transfer to drops of liquid in the spheroidal state. Ph.D. Thesis, Purdue University, West Lafayette, IN (1953).
6. K. H. Baumeister, T. D. Hamil and G. J. Schoessow, A generalized correlation of vaporization times of drops in

film boiling on a flat plate, in *Third Int. Heat Transfer Conf.* Chicago, IL, Vol. 4, pp. 66–73 (1966).
7. L. H. Wachters and N. A. J. Westerling, The heat transfer from a hot wall to impinging water drops in the spheroidal state, *Chem. Engng Sci.* **21,** 1047–1056 (1966).
8. L. Bolle and J. C. Moureau, Spray cooling of hot surfaces, in *Multiphase Science and Technology* (edited by G. F. Hewitt, J. M. Delhaye and N. Zuber) pp. 1–92. Hemisphere, New York (1976).
9. F. Akao, K. Araki, S. Mori and A. Moriyama, Deformation behaviors of a liquid droplet impinging onto hot metal surface, *Trans. Int. Steel Inst. Japan* **20,** 737–743 (1980).
10. P. Savic and G. T. Boult, The fluid flow associated with the impact of liquid drops with solid surfaces. National Research Laboratories of Canada, MT-26, Ottawa, Canada (1955).
11. S. Toda, A study of mist cooling (1st report: Investigation of mist cooling), *Heat Trans. Jap. Res.* **1,** 39–50 (1972).
12. O. G. Engel, Water drop collisions with solid surfaces, *J. Res. NBS* **54,** 281–298 (1955).
13. M. Kurokawa and S. Toda, Heat transfer of an impacted single droplet on the wall, in *Proceedings of the ASME/JSME Thermal Engineering Joint Conf.* (edited by J. R. Lloyd and Y. Kurosaki), Vol. 2, pp. 141–146 (1991).
14. S. Chandra and C. T. Avedisian, On the collision of a droplet with a solid surface, *Proc. R. Soc. Lond.* **432,** 13–41 (1991).
15. J. Senda, K. Yamada, H. Fujimoto and H. Miki, The heat transfer characteristics of a small droplet impinging upon a hot surface, *JSME Int. J.* **31,** 105–111 (1988).
16. K. Makino and I.Michiyoshi, The behavior of a water droplet on heated surfaces, *Int. J. Heat Mass Transfer* **27,** 781–791 (1984).
17. K. Takeuchi, J. Senda and Y. Sato, Experimental studies on the behavior of a small droplet impinging upon a hot surface, in *Proceedings of the Second Int. Conf. on Liquid Atomization and Spray Systems*, Madison, WI, pp. 397–404 (1982).
18. S. Chandra and C. T. Avedisian, Observations of droplet impingement on a ceramic porous surface, *Int. J. Heat Mass Transfer* **35,** 2377–2388 (1992).
19. I. Mudawar and W. S. Valentine, Determination of the local quench curve for spray cooled metallic surfaces, *ASM J. Heat Treating* **7,** 107–121 (1989).
20. P. J. Halvorson, R. J. Carson, S. M Jeter and S. I. Abdel-Khalik, Critical heat flux limits for a heated surface impacted by a stream of liquid droplets, *J. Heat Transfer* **116,** 679–685 (1994).
21. S. Inada and W. J. Yang, Mechansisms of miniaturization of sessile drops on a heated surface, *Int. J. Heat Mass Transfer* **36,** 1505–1515 (1993).
22. C. O. Pedersen, An experimental study of the dynamic behavior and heat transfer characteristics of water droplets impinging upon a heated surface, *Int. J. Heat Mass Transfer* **13,** 369–381 (1969).